



HAL
open science

Investigation of the anisotropic strain relaxation in GaSb islands on GaP

Y. Wang, P. Ruterana, H.P. Lei, Jie Chen, S. Kret, S. El Kazzi, L.
Desplanque, X. Wallart

► **To cite this version:**

Y. Wang, P. Ruterana, H.P. Lei, Jie Chen, S. Kret, et al.. Investigation of the anisotropic strain relaxation in GaSb islands on GaP. *Journal of Applied Physics*, 2011, 110, pp.043509-1-8. 10.1063/1.3622321 . hal-00639828

HAL Id: hal-00639828

<https://hal.science/hal-00639828>

Submitted on 25 May 2022

HAL is a multi-disciplinary open access archive for the deposit and dissemination of scientific research documents, whether they are published or not. The documents may come from teaching and research institutions in France or abroad, or from public or private research centers.

L'archive ouverte pluridisciplinaire **HAL**, est destinée au dépôt et à la diffusion de documents scientifiques de niveau recherche, publiés ou non, émanant des établissements d'enseignement et de recherche français ou étrangers, des laboratoires publics ou privés.

Investigation of the anisotropic strain relaxation in GaSb islands on GaP

Cite as: J. Appl. Phys. **110**, 043509 (2011); <https://doi.org/10.1063/1.3622321>

Submitted: 25 February 2011 • Accepted: 04 July 2011 • Published Online: 18 August 2011

Y. Wang, P. Ruterana, H. P. Lei, et al.



View Online



Export Citation

ARTICLES YOU MAY BE INTERESTED IN

[Strain relief at the GaSb/GaAs interface versus substrate surface treatment and AlSb interlayers thickness](#)

Journal of Applied Physics **109**, 023509 (2011); <https://doi.org/10.1063/1.3532053>

[The source of the threading dislocation in GaSb/GaAs hetero-structures and their propagation mechanism](#)

Applied Physics Letters **102**, 052102 (2013); <https://doi.org/10.1063/1.4790296>

[Mechanism of formation of the misfit dislocations at the cubic materials interfaces](#)

Applied Physics Letters **100**, 262110 (2012); <https://doi.org/10.1063/1.4731787>

Lock-in Amplifiers
up to 600 MHz



Zurich
Instruments



Investigation of the anisotropic strain relaxation in GaSb islands on GaP

Y. Wang,^{1,a)} P. Ruterana,¹ H. P. Lei,¹ J. Chen,² S. Kret,³ S. El Kazzi,⁴ L. Desplanque,⁴ and X. Wallart⁴

¹CIMAP, UMR 6252 CNRS-ENSICAEN-CEA-UCBN, 6, Boulevard du Maréchal Juin, 14050 Caen Cedex, France

²LRPMN, EA4257, Université de Caen, IUT d'Alençon, Damigny, France

³Institute of Physics, PAS, AL. Lotników 32/46, 02-668 Warszawa, Poland

⁴Institut d'Electronique, de Microélectronique et de Nanotechnologie, UMR-CNRS 8520, BP 60069, 59652 Villeneuve d'Ascq Cedex, France

(Received 25 February 2011; accepted 4 July 2011; published online 18 August 2011)

The strain relaxation at the initial stages of highly mismatched (11.8%) GaSb grown on a GaP substrate following a Ga-rich surface treatment by molecular beam epitaxy has been investigated. High resolution transmission electron microscopy and moiré fringe analysis were used to determine the relaxation state in these GaSb islands in the [110] and [1–10] directions. The measurements revealed an anisotropic strain relaxation in these two directions; there is a higher misfit strain relaxation along the [110] direction where the islands are elongated, which is in agreement with a higher density of misfit dislocations. By combining molecular dynamics simulations and TEM results, the anisotropy in the strain relaxation is shown to be related to the asymmetry in the formation of interface misfit dislocations. The P-core glide set 60° dislocations (α type) and the Ga-core shuffle set Lomer dislocations serve as the primary misfit dislocation which contributes to the strain relaxation in the (1–10) interface, and the Ga-core glide set 60° dislocations (β type) and the P-core shuffle set Lomer dislocations for the (110) interface, respectively. The lower formation energy and higher glide velocity of the P-core glide set 60° dislocations (α type) result in a higher line density and more uniform periodical distribution of the misfit dislocation in the (1–10) interface. The higher fraction of Lomer dislocations, which is related to the dislocation configuration stability and surface treatment, promotes a better strain relief in the (1–10) interface, with a corresponding elongation of islands in the [110] direction. © 2011 American Institute of Physics. [doi:10.1063/1.3622321]

I. INTRODUCTION

Antimony-based compounds offer a wide range of electronic bandgaps and band offsets along with extremely high electron mobility, therefore enabling a variety of devices that are much faster with lower power consumption.¹ However, the strain and high density of defects due to the large lattice mismatch between the III-Sb epitaxial layers and substrate (e.g., GaAs, GaP, and Si) has, until now, plagued both the electrical and optical properties of the devices. The research on strain relaxation in III-V semiconductor heterostructures has been very active,^{2,3} which has a significant impact on the electrical and optical properties. Since the III-V compound semiconductors have a zinc blende lattice which is noncentrosymmetric, orthogonal directions such as the in-plane $\langle 110 \rangle$ directions at the (001) interface are not equivalent. In GaSb, for instance, the (110) plane has Sb-terminated {111} facets, whereas the (1-10) plane exhibits Ga-terminated ones. Anisotropies in the electrical and optical properties of III-V compound semiconductor materials and devices fabricated in the [110] and [1–10] in-plane directions are often observed.^{4,5} However, the electronic band structures in the $\langle 110 \rangle$ in-plane directions are equivalent and thereby, differences in the properties along the two directions are expected to arise from an asymmetry strain relaxation or extrinsic

defect-related source. Looking back at the extensive reports of the III-V compound semiconductor,^{4–10} many were on small mismatched (for instance less than 1%) systems. For binary-binary epitaxial systems, it has been reported that the lattice mismatch plays a decisive role in the configuration of the interface misfit dislocation. More precisely, low strain systems ($< 2\%$) lead to 60° dislocations, moderate strain (3–4%) in mixed Lomer and 60° dislocations, and high strain ($> 6\%$) in pure Lomer.^{11,12} However, Narayan *et al.* report¹³ and our previous work¹² have shown that the misfit dislocations network predominately consisted of 90° pure edge dislocations and closely spaced 60° dislocation pairs in high mismatch systems. Moreover, the closely spaced 60° dislocation pairs may not vanish even by surface treatment¹² or post-annealing.¹³ However, also exhibiting a large mismatch, InAs has been shown to behave differently upon growth on GaAs or GaP: both coherent strain (misfit dislocation free)^{14,15} and plastic relaxation^{16,17} have been reported. Therefore, in the high mismatched systems, the configurations and formation mechanisms of the interface misfit dislocations are complex and may need further investigation.

In this work, using transmission electron microscopy (TEM) in combination with geometrical phase analysis (GPA) method, we investigate the anisotropic strain relaxation of highly mismatched (11.8%) GaSb islands grown on a GaP substrate by molecular beam epitaxy (MBE), initiating the growth with one monolayer (ML) Ga at 480 °C. Moreover,

^{a)}Electronic mail: yi.wang@ensicaen.fr.

molecular dynamics based on Stillinger-Weber (SW) potentials¹⁸ have been carried out to investigate the atomic configuration and stability of the interface misfit dislocations.

II. EXPERIMENT

A. Experimental procedures

The investigated samples were grown by MBE on (001) GaP substrates in a Riber 32P chamber equipped with group III and V sources. The phosphorous flux was obtained by cracking phosphine (PH_3) through a high-temperature injector, whereas a valve-cracker cell was used to produce Sb_2 . The Ga and Sb fluxes were calibrated via reflection high energy electron diffraction (RHEED) specular beam intensity oscillations on GaP and GaSb. Following the deoxidization of the GaP substrates at 650 °C, a 400 nm GaP buffer layer was grown at 610 °C to obtain a smooth GaP surface exhibiting a sharp (2×4) RHEED pattern. Afterwards, the phosphine flux was interrupted and the substrate was cooled down from 610 to 480 °C without any flux, keeping a (2×4) surface reconstruction. Then 1 ML Ga was deposited before the opening of the Sb valve with a subsequent growth of 9 GaSb MLs. A growth rate of 0.7 ML/s was used during the antimonide layer growth. The surface morphology of the samples was examined by atomic force microscopy (AFM) using a Digital Nanoscope III system, working in the tapping mode. For TEM observations, the sample's preparation was achieved using conventional mechanical polishing and dimpling with a final step of ion milling. The argon ion milling was performed at -150 °C in order to minimize ion beam damage. Both $[110]$ and $[1\bar{1}0]$ cross-section specimens were observed in two JEOL microscopes: a 2010 FEG for HRTEM analysis and a 2010LaB₆ for conventional TEM, both operated at 200 kV.

B. Experimental results

The surface morphology of the GaSb islands were characterized by AFM. The AFM image (Fig. 1) revealed that the island density was around $1.8 \times 10^{10}/\text{cm}^2$, the average island height was about 6.5 nm, and all the islands were elongated along the $[110]$ direction. Figure 2 shows a bright field cross-section TEM of the GaSb islands in two perpendicular directions. The average (more than 40 islands) height of the islands is 8.0 ± 1.4 nm, which is slightly larger than the AFM result. The small islands have a round and lens-shaped form. The largest islands always have flat surfaces and $\{111\}$ side facets (indicated by a red line in Fig. 1). In addition, the island's base length along the $[110]$ direction is larger than along the $[1\bar{1}0]$ direction. This result is consistent with the AFM observation, which indicates that in our case, the Ga-terminated $\{111\}$ facets moves forward more than the Sb-terminated $\{111\}$ ones. In the literature, the island's elongation along $[1\bar{1}0]$ ^{19,20} and $[110]$ ^{21,22} has been reported and the elongated island shapes are often attributed to the anisotropy of the diffusion length of adatoms or the growth speed along different crystallographic direction.²³

Figure 3(a) shows a plane-view TEM images of 9 MLs of GaSb grown on GaP in the $[001]$ zone axis. This image

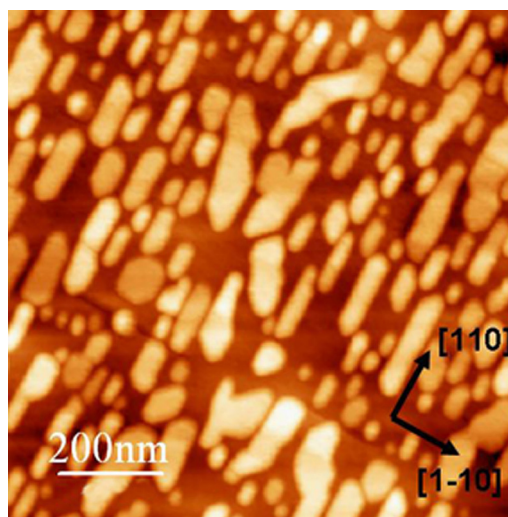


FIG. 1. (Color online) AFM image of GaSb islands on GaP. The islands are systematically elongated in the $[110]$ direction.

reveals that the GaSb islands have a random shape, however, they all elongated along the $[110]$ direction. Figure 3(b) shows a selected area electron diffraction (SAED) pattern which includes many (>100) islands. The highly-resolved diffraction spots in the SAED demonstrate two separate lattices constants associated with GaP (5.4512 Å) and GaSb (6.0959 Å), respectively. Besides the spots corresponding to GaP and GaSb, some additional spots present in the diffraction patterns are produced by double diffraction (DD).²⁴ For instance, considering the $(0-40)$ diffraction spots, the different color spots show the classification of the diffraction spots in Fig. 3(b). The alignment of the (000) diffraction spot with, for instance, the (200) spots indicates that there is no lattice rotation between the GaSb islands and GaP substrate. As measured from the SAED, the interplanar spacing ratio of the (220) to $(2\bar{2}0)$ is about 1.03, indicating a macro-anisotropic (about 3%) strain relaxation in the two directions. In order to verify this, we use the moiré fringe patterns to

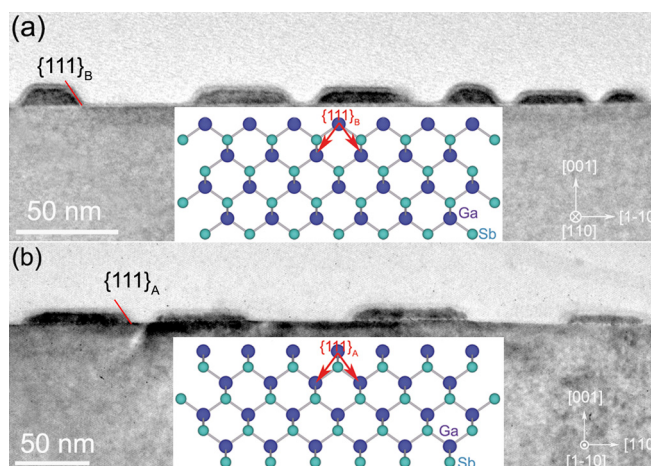


FIG. 2. (Color online) Cross-sectional bright field TEM micrographs of 9 MLs of GaSb grown on GaP along the two perpendicular directions: (a) the $[110]$ direction, and (b) the $[1\bar{1}0]$ direction. The insets of (a) and (b) are the $[110]$ and $[1\bar{1}0]$ projections of the GaSb cell. The (110) and $(1\bar{1}0)$ interfaces have Sb-terminated $\{111\}$ and Ga-terminated $\{111\}$ facets, respectively.

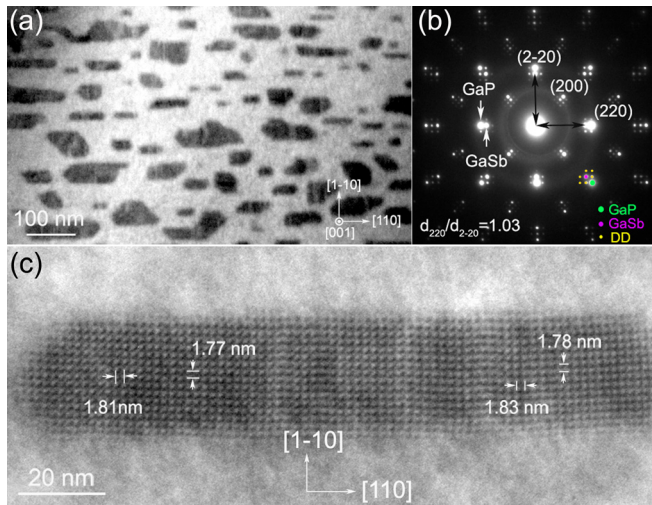


FIG. 3. (Color online) (a) Plane-view TEM image of 9 MLs of GaSb grown on GaP in the [001] zone axis, illustrating that the GaSb islands are elongated in the [110] direction. (b) The corresponding selected area electron diffraction (SAED) pattern. The different size (color) spots show classification of the (0–40) diffraction; large (green), medium (red), and small (yellow) spots correspond to GaP, GaSb, and double diffraction (DD), respectively. (c) The [001] bright field image showing the (220) and (2–20) moiré fringes.

map the relaxation of an individual island, which is very sensitive for evaluating the lattice parameter of the epitaxial layer relative to that of the substrate.^{25,26} Figure 3(c) shows the two dimensional moiré fringes of a typical island with a dimension of $50 \times 145 \text{ nm}^2$, as viewed along the [001] zone axis in the bright field. The spacing of the moiré fringes is given by $D = d_e d_s / (d_e - d_s)$, where d_e and d_s are the corresponding d spacings of the overlapping planes of the epilayer and the substrate, respectively. Applying this equation to a relaxed GaSb on GaP, the ideal spacing $D_{\{110\}}$ is 1.83 nm. As shown in the figure, the measured [110] moiré fringe spacing is slightly larger than that of the [1–10] direction; moreover, it is closer to the ideal result, indicating that the island is more relaxed in the [110] direction.

To clarify this discrepancy, we carried out a detailed cross-sectional HRTEM analysis in both the [1–10] and [110] directions. Figure 4 shows HRTEM images of the (110) [Fig. 4(a)] and (1–10) [Fig. 4(b)] interfaces between the GaSb islands and the GaP substrate. In these images, the positions of the interface dislocations have been marked by the additional {111} lattice planes (inclined arrows). The extra half planes of the misfit dislocations are observed in the GaP substrate because the lattice constant of GaSb is larger than that of the GaP substrate. Lomer 90° dislocations, close 60° dislocation pairs, and isolated 60° dislocations can be seen along the interface. These defects are the major interfacial defects which accommodate the misfit strain. Some important features in these images need to be pointed out; as can be seen, the closely spaced 60° dislocation pairs always lie in the intersecting glide planes but very rarely in parallel glide planes, and the isolated 60° dislocations appear to form toward the edge of the island. For the present images, the average spacing of the Lomer dislocations are 3.78 and 3.62 nm for Figs. 4(a) and 4(b), respectively. Compared to the

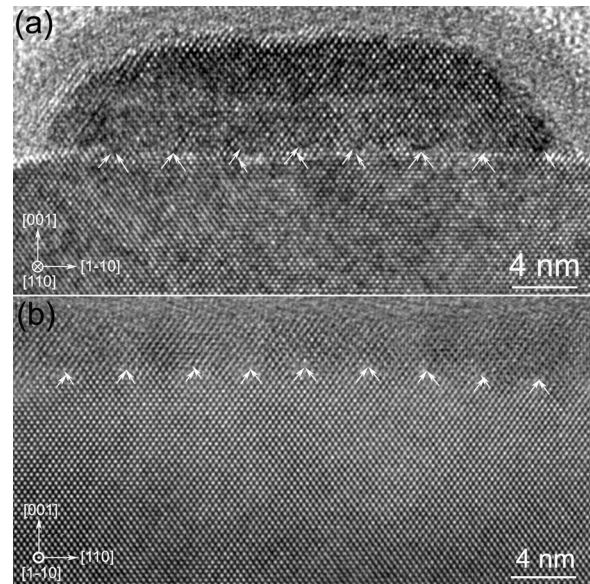


FIG. 4. HRTEM images of the GaSb islands on the GaP substrate observed along the [110] and [1–10] orientation; inclined arrows indicate extra {111} planes at the interface. The average distances of interface misfit dislocation are (a) 3.78 nm, and (b) 3.62 nm in two perpendicular directions, respectively.

theoretical value (3.65 nm) for the GaSb/GaP system, we have a small residual strain of about 3.6 and 0.7% for the [1–10] and [110] directions, respectively. The 2.9% discrepancy of the strain relaxation in the two perpendicular directions is consistent with the SAED observation discussed in the preceding text.

We apply the geometrical phase analysis (GPA) of HRTEM to investigate the local strain distribution as along with the arrangement of the interface dislocations.^{12,27,28} Figure 5 shows the ϵ_{xx} component of the strain field (deformation along the [001] growth direction) derived from Fig. 4. In these images, the dislocation cores are easily

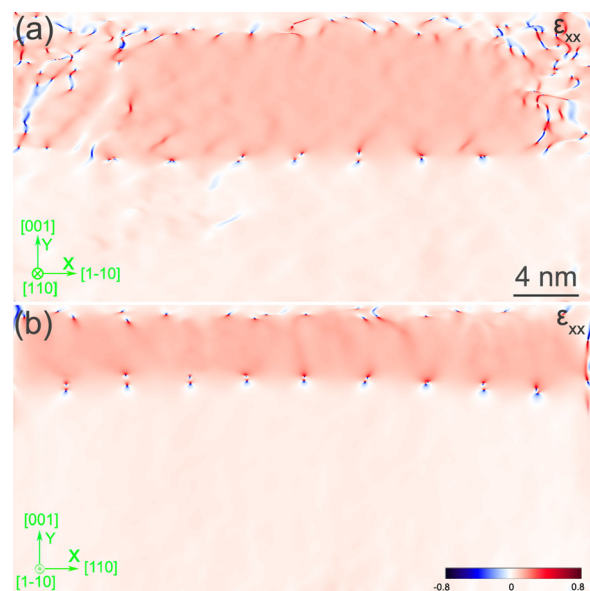


FIG. 5. (Color online) Strain ϵ_{xx} maps corresponding to the Fig. 4 HRTEM images. The dislocation cores are now clearly marked by areas of highest local strain at the interfaces.

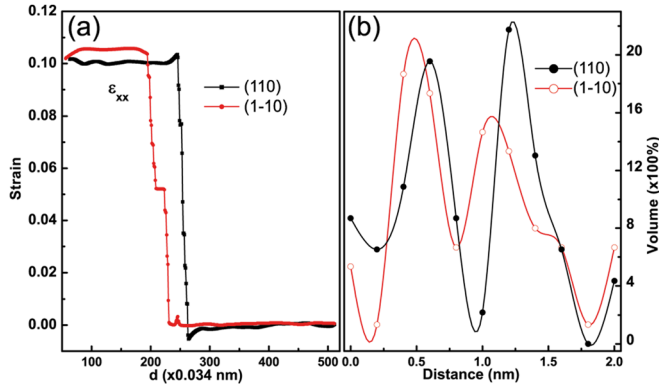


FIG. 6. (a) (Color online) The corresponding projection of the ϵ_{xx} images on the growth direction. The vertical part of each curve shows the interfacial layer thickness and the maximum height corresponds to the relaxation level. (b) Statistical distribution of the distance between the cores of misfit dissociated dislocations in the two interfaces (two peaks are present in each curve: they correspond to the split cores of the Lomer and 60° pair dislocations, respectively).

delineated at the nanometer scale: they correspond to the areas where the strain is maximal. In these areas, most of the Lomer dislocations are split at the nanometer scale distance in two 60° dislocations, as shown by the core positions. Projecting the strains onto the growth direction allows us to calculate the average relaxation state of the layers. As shown in Fig. 6(a), the ϵ_{xx} in the (110) interface is larger than the (1-10), which is indicative of a distinct anisotropy of strain relaxation along two orthogonal $\langle 110 \rangle$ directions in the (001) plane.

From a large number of HRTEM images (with more than 50 pairs of dislocations for each direction) combined with GPA, we have estimated the probability of different misfit dislocation configurations in the (110) and (1-10) interfaces as summarized in Table I. We define a pure Lomer dislocation as being characterized by two additional intersecting lattice planes and a splitting 60° dislocation core less than 1 nm, and 60° dislocation pairs, which we consider as the core spacing is larger than 1 nm. The average spacing of the Lomer dislocation in the (1-10) interface almost coincides with the theoretical value of 3.65 nm, corresponding to a better strain relief along [110], as we have previously discussed. The fraction of three proposed misfit dislocation configurations reveals that Lomer dislocations are the dominant defects for the strain relaxation.

Besides the strain distribution and the types of the interface misfit dislocation, the fine structure of the dislocation core has also been analyzed. The distance between dissociated cores for the Lomer dislocations and 60° dislocation

TABLE I. Statistics (with more than 50 pairs of dislocation for each direction) about the interface misfit dislocation.

Interface	Spacing of Lomer dislocation	Line density of the interface dislocation (cm^{-1})	Fraction		
			Lomer (%)	60° pairs (%)	60° (%)
(110)	3.80 ± 0.20	5.5×10^3	55.3	42.6	2.1
(1-10)	3.65 ± 0.06	7.0×10^3	60	37.5	2.5

pairs, as determined in many areas, is presented in Fig. 6(b). Obviously, the cores in the (110) interface are more localized, both for the Lomer dislocation and 60° dislocation pair.

III. MODELING

A. Theoretical procedures

The Stillinger-Weber (SW) potentials¹⁸ have been used extensively to model the structural properties of the tetrahedral semiconductors. They have been used to simulate distorted and broken bond systems. In recent years, they have even been extended to the wurtzite semiconductors for modeling the structure of various extended defects.^{29,30} Explicitly, SW potentials are based on a two-body term and three-body term interaction of the nearest neighbor atoms,

$$\Phi(1, \dots, N) = \sum_{i,j(i<j)}^N \phi_2(i, j) + \sum_{i,j(k)}^N \phi_3(i, j, k). \quad (1)$$

The two-body interaction term is

$$\phi_2(i, j) = \epsilon f_2(r_{ij}/\sigma), \quad (2)$$

with

$$f_2(r) = \begin{cases} A(B/r^4 - 1) \exp[1/(r - a)], & r < a, \\ 0, & r > a, \end{cases} \quad (3)$$

and the three-body interaction term is

$$\begin{aligned} \phi_3(i, j, k) &= \epsilon f_3(\vec{r}_i/\sigma, \vec{r}_j/\sigma, \vec{r}_k/\sigma), \\ f_3(\vec{r}_i, \vec{r}_j, \vec{r}_k) &= h(r_{ij}, r_{jk}, \theta_{ijk}) + h(r_{ji}, r_{jk}, \theta_{ijk}) + h(r_{jk}, r_{ki}, \theta_{jki}), \end{aligned} \quad (4)$$

$$\begin{aligned} h_{ijk}(r_{ij}, r_{jk}, \theta_{ijk}) &= \lambda \exp[\gamma/(r_{ij} - a) + \gamma/(r_{jk} - a)] \\ &\quad \times (\cos \theta_{ijk} + 1/3)^2, \end{aligned}$$

where ϵ and δ are energy and length units, respectively, a is the cut-off distance, $\theta(i, j, k)$ is the angle formed by the \vec{r}_{ij} and \vec{r}_{jk} vectors, and A , B , λ , and γ are the bond strength factors.

During the molecular dynamics simulation only the nearest neighbors are considered. The parameters of the Stillinger-Weber potential have been reported by Ichimura³¹ and Wang *et al.*,³² and they are summarized in Table II. Besides the normal bonds, Ga-P and Ga-Sb, the wrong bonds Ga-Ga, P-P, and Sb-Sb have also been considered. Since there are no proper valid parameters available for the wrong bonds, as has already been done by Zhou *et al.*,³³ we adopt

TABLE II. The S-W potential parameters for the molecular dynamic simulation.

Bond	d (Å)	ϵ (eV)	A	B	δ (Å)	λ
Ga-P	2.36	1.78	7.62333	0.681	2.0642	29.57
Ga-Sb	2.64	1.48	7.91549	0.720	2.2900	32.49
Ga-Ga	2.44	1.63	5.9768	0.5860	2.183	21
As-As	2.50	1.63	6.8553	0.6711	2.183	21

the parameter of GaAs to replace them. The Lomer misfit dislocation is constructed in a series of supercells with various sizes in the xy plane [(001) plane], $32a \times 32a$ for GaSb and $36a \times 36a$ for GaP (a : corresponding lattice constant for GaP and GaSb), respectively. The supercells are made up of 30 monolayers of GaSb sandwiched between two 20 monolayers of GaP along the z direction, and they contain 82 560 atoms. The relaxation procedures are performed using the quench algorithm³⁴ and they are stopped when the system kinetic temperature is lower than 10^{-8} K.

B. Simulation results

In III-V cubic compounds, the dislocations are expected in $\{111\}$ planes with their Burgers vectors along the $\langle 110 \rangle$ direction. Two atomic structures of the Lomer dislocation in diamond structure were proposed by Hornstra.³⁵ The first one, namely the shuffle set, consists of structural units of five- and seven-fold rings. The other structure consists of a eight-atom rings with an inner atom and two dangling bonds or an eight-fold ring superimposed on a six-fold ring, corresponding to the glide set. The dislocation cores in the III-V compounds consist of either III or V elements; therefore, there are four types of Lomer dislocations, namely the shuffle set with the III or V element core and the glide set with the III or V element core. Our simulation results show that the Ga core dislocation tends to form on the substrate with a Ga-terminated (001) surface, whereas the P core dislocation will occur on a P-terminated (001) surface.

Figure 7(a) schematically shows the arrangement of Lomer dislocations for the GaSb ($32a \times 32a$)/GaP ($36a \times 36a$) heterostructure. Figures 7(b) and 7(c) show the $[1-10]$ and $[110]$ cross-section projection of a quarter of the simulated GaSb on Ga-terminated (001) GaP. For a fully relaxed GaSb on a GaP substrate with an ideal Ga-terminated (001) surface, to minimize the system energy, the shuffle set Lomer dislocations lie along $[1-10]$ direction and have $a/2$ $[110]$ Burgers vector. In contrast, the glide set Lomer dislocations rotate 90° , and they lie along the $[110]$ direction and have $a/2$ $[1-10]$ Burgers vector. Furthermore, all of the dislocations have a Ga core; specifically, their $\{111\}$ additional planes are terminated with Ga atoms. The two sets of Lomer dislocations are periodically distributed at the interface, and each shuffle (glide) set Lomer dislocation is surrounded by 4 glide (shuffle) set Lomer dislocations, as schematically shown in Fig. 7(a). Due to this configuration, for the ideal heterostructure in the cross-section we can only observe one set of Lomer dislocations; the other set will be out of contrast. Similarly, for the GaP substrate with an ideal P-terminated (001) surface, the Lomer misfit dislocations have the same arrangement. Namely, the P-core shuffle set Lomer dislocations lie along the $[110]$ direction and have $a/2$ $[1-10]$ Burgers vector, while the P-core glide set Lomer dislocations lie along $[1-10]$ direction and have $a/2$ $[110]$ Burgers vector, as shown in Figs. 7(d) and 7(e).

To estimate the energy of the four types of Lomer dislocations, we consider a heterostructure with only one Lomer dislocation. We pick up 4 super-cells with same size of GaSb/GaP from the inner part of the GaSb ($32a \times 32a$)/GaP

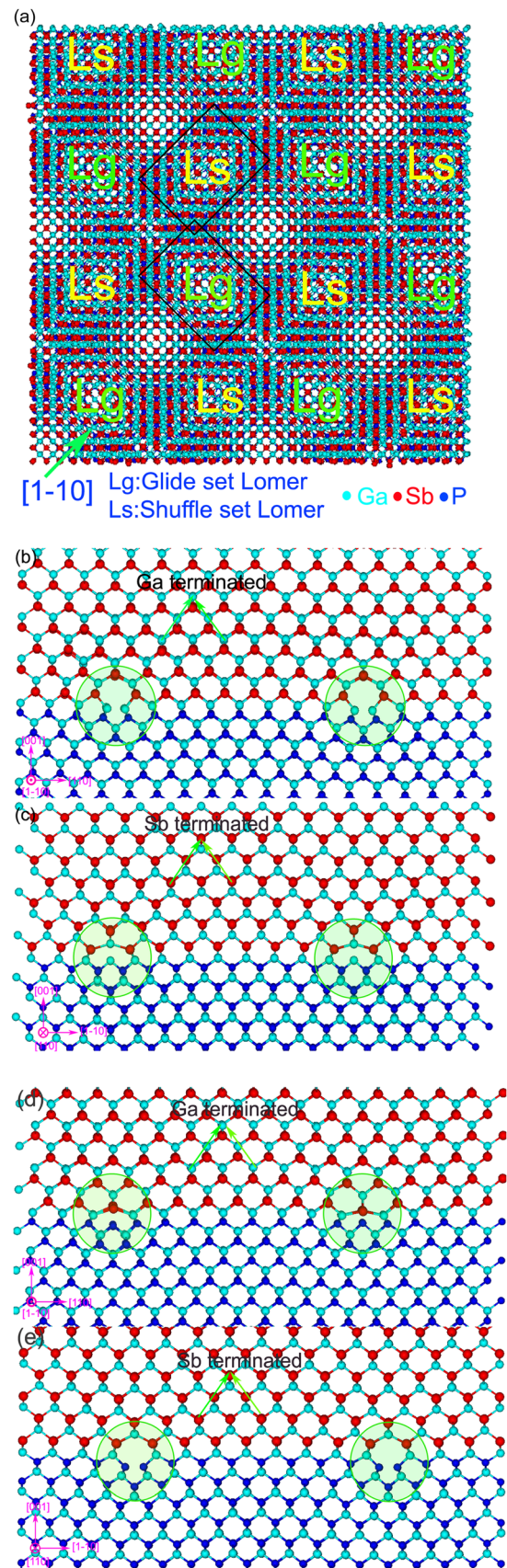


FIG. 7. (Color online) (a) The $[001]$ projection of the GaSb($32a \times 32a$)/GaP($36a \times 36a$) heterostructure shows the configuration of the Lomer dislocation at the interface. The (b) $[1-10]$, and (c) $[110]$ cross-section projection of a quarter of the simulated GaSb on Ga-terminated (001) GaP. The (d) $[1-10]$, and (e) $[110]$ cross-section projections of a quarter of the simulated GaSb on the P-terminated (001) GaP.

(36a × 36a) heterostructure, as indicated by the black rectangles in Fig. 7(a). For each rectangle, their symmetry line cuts through the center of the dislocation (one along the dislocation line, and the other perpendicular to the dislocation line). These super-cells have the same shape and atoms; moreover, each super-cell contains only one Lomer dislocation, Ga-core shuffle set, Ga-core glide set, P-core shuffle set, or P-core glide set, respectively. The total elastic energy of the four super-cells, is as follows: P-core glide set > Ga-core glide set > Ga-core shuffle set > P-core shuffle set. These results qualitatively indicate the energy tendency of the four types of Lomer dislocations. Besides the total energy of the relaxed structure, the molecular dynamics calculations also provide the total energy projected onto a single atom, j . The energy of the single atom, j , is then defined as the difference between the total energy, E_{tot}^j , and the total energy of the same type of atom in a perfect material, $E_{\text{tot}}^{\text{bulk}}$:

$$E_f^j = E_{\text{tot}}^j - E_{\text{tot}}^{\text{bulk}}. \quad (5)$$

Here, $E_{\text{tot}}^{\text{bulk}}$ is determined in a bulklike super-cell cluster of the same shape as the dislocated models. There is no valid value at the GaSb/GaP interface; for instance, some Ga atoms form bonds with both Sb and P. In this case, the $E_{\text{tot}}^{\text{bulk}}$ is replaced by the average between the GaSb and GaP ($\frac{1}{2}[E_{\text{tot}}^{\text{bulk}}(\text{GaSb}) + E_{\text{tot}}^{\text{bulk}}(\text{GaP})]$). From an analysis of the atomic energy distribution of such super-cells, we notice that the energy of the atoms away from the dislocation core is almost zero. Thus, projecting all the atoms energy (E_f^j) along the Z axis ([001] direction) of the selected super-cells will give us the energy distribution at the dislocation core region. Figures 8(a) and 8(c) show the energy distribution along and perpendicular to the dislocation line, and they reveal the energy and width of the four types of Lomer dislocations. To quantify these results, Fig. 8(b) shows the linear fitting of the curves in Fig. 8(a), the inset table of Fig. 8(c) summarizes the full width at half maximum (FWHM), and the integrated value of the curves in Fig. 8(c). Obviously, the P-core glide set Lomer dislocation has much higher energy in comparison with other types of Lomer dislocations. In terms of the FWHM, we can see that the shuffle set dislocation has a more compact core than the glide set. From this analysis, it can be concluded that the shuffle set Lomer dislocations are more stable than the glide set. Moreover, besides the core configuration, the core element is the key factor in the determination of the dislocation energy. This may more or less explain the discrepancy of 5% in the fraction of the Lomer dislocation in the (110) and (1-10) interfaces.

IV. DISCUSSION

In the following, we discuss the origin of the discrepancy in strain relaxation in the two [110] and [1-10] directions. For the Lomer dislocation, there are two sets of 60° dislocations, which belong to the glide set if their motion leads to shear between two narrowly spaced {111} planes, or to the shuffle set if the shear is between two widely spaced {111} planes. Regarding the core element, there are also

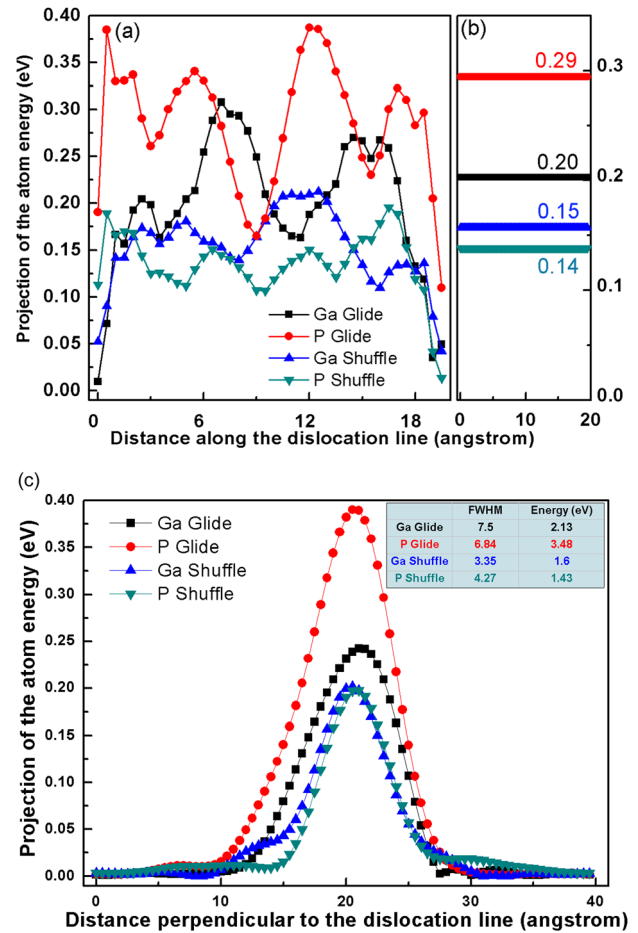


FIG. 8. (Color online) (a) The energy distribution of four types of Lomer dislocations obtained by projecting the atom energy perpendicular to the dislocation line, and (b) the corresponding linear fitting. (c) The energy distribution perpendicular to the dislocation line of four types of Lomer dislocations obtained by projecting the atom energy along the dislocation line.

four possible types of 60° dislocations, namely III-core shuffle set, III-core glide set, V-core shuffle set, and V-core glide set, respectively. We have illustrated their configuration in Fig. 8. In many reports, the V-core and III-core 60° dislocations have been named α and β type dislocations.^{36,37}

As we previously mentioned, in a compressive epitaxial layer the extra half plane of the interface dislocation must be in the substrate to relieve strain. It can be seen in Fig. 9 that, in order to do so, the III-core shuffle set and V-core glide set 60° dislocation will lie in the [1-10] direction (dislocation line direction); similarly, the V-core shuffle set and III-core glide set 60° dislocation must lie in the [110] direction. Concerning their motion, {111} is the slip plane and the glide set dislocations are the predominantly mobile dislocations.^{38,39} Thus, the V-core glide set and III-core glide set dislocation should be the highest density 60° dislocations during the observations. Moreover, the V-core glide set (α type) 60° dislocations have been shown to have a lower formation energy and higher glide velocity,^{37,38,40} in comparison with III-core (β type).

Recalling the formation process of the misfit dislocation,^{13,41} in a lens-shape island grown in the three-dimensional mode, the first 60° dislocations are generated as half loops

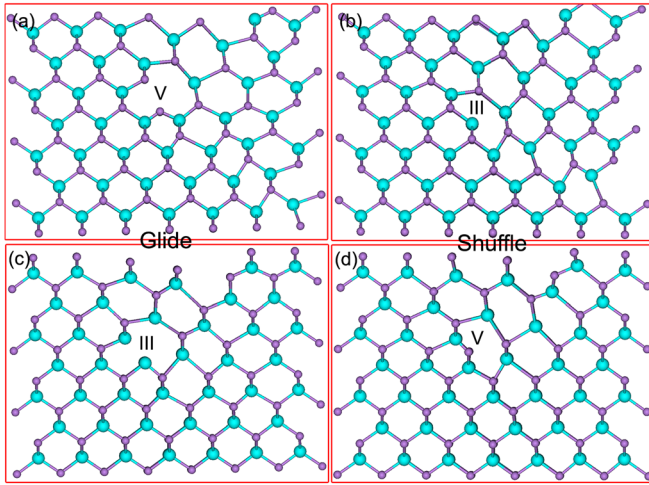


FIG. 9. (Color online) The configuration of the four 60° dislocations in bulk III-V compounds: (a) V-core glide set, (b) III-core shuffle set, (c) III-core glide set, and (d) V-core shuffle set.

after the island reaches a critical size, then the nucleated dislocation half loops glide toward the interface and form misfit segments. After the first set of misfit dislocations is formed and the misfit strain is partially relaxed, the second set of 60° dislocations will nucleate in the net stress field formed by the residual misfit. Subsequently, the second set of 60° dislocations also glides to the interface. If the two sets of 60° dislocations have opposite screw components they will react to a 90° (or Lomer) dislocation³⁵ [as schematically shown in Fig. 10(a), $b_{1s} = -b_{2s}$], otherwise, they probably give rise, at most, to a closely spaced 60° pair as their parallel screw component prohibits their combination [Fig. 10(b), $b_{1s} = b_{2s}$]. In fact, both pairs (with an opposite screw component and with a parallel screw component) exhibit attractive interaction, however, the attraction in the pair with the opposite screw component is 10 times larger than that in the pair with the parallel screw component.⁴² After forming the Lomer dislocation, 60° dislocation pairs, and an isolated 60° dislocation, they can be slightly redistributed by a glide and climb motion along the interface. Since P-core 60° dislocations have higher glide velocity, they glide more efficiently to the interface, thus more interface dislocations will appear in the (1–10) interface. This is consistent with our statistical observations: the line density of the interface misfit dislocation in the (1–10) interface is $7.0 \times 10^3 \text{ cm}^{-1}$, whereas it is $5.5 \times 10^3 \text{ cm}^{-1}$ for the (110) interface. Similarly, we also observe that the higher glide velocity of α type dislocations result in more localized cores, as we have shown in Fig. 6(b). In fact, the edge component of the second set of 60° dislocations is controlled by the stress field of the first set of 60° dislocations,¹³ so for the closely spaced 60° dislocation pairs only an intersecting glide plane can be found at the interface region, as we previously mentioned.

Based on our simulation, for the Lomer dislocation, the shuffle set dislocations are more energetically favorable than the glide set. Thus, the 60° dislocations tend to form the shuffle set Lomer dislocation during their combination process. Regarding their arrangement, the P-core shuffle set dislocation should dominate the Lomer dislocation density in the (110) interface and the Ga-core shuffle set Lomer dislo-

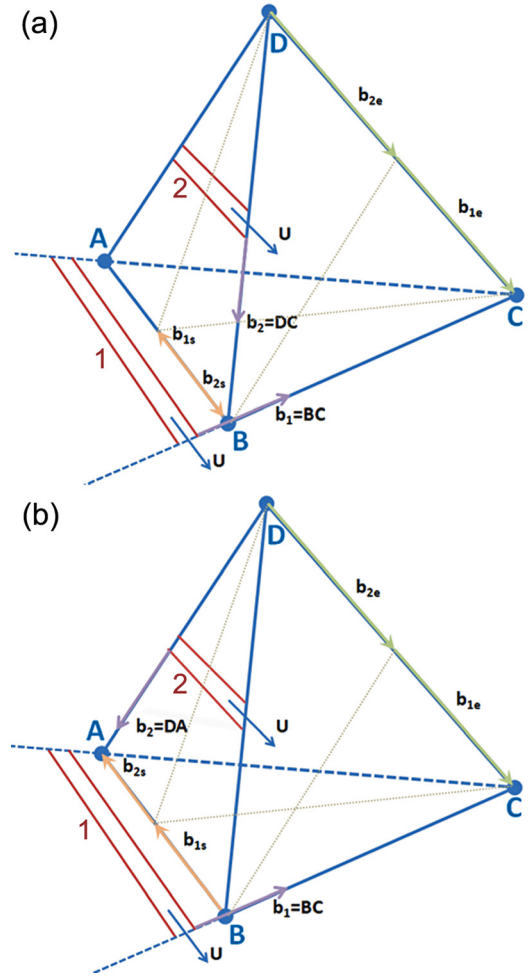


FIG. 10. (Color online) A diagram of the reaction of two 60° dislocations using the Thompson tetrahedron: (a) the Lomer dislocation, and (b) a closely spaced 60° dislocation pair. Here, U and b indicate the dislocation line and Burgers vectors direction; b_{1s} , b_{1e} , b_{2s} , and b_{2e} represent the screw and edge components of the first and second dislocations, respectively.

cation in the (1–10) interface. However, due to the small energy difference between the P-core shuffle set and the Ga-core glide set Lomer dislocations, and since our initial growth starts with the Ga-rich surface, the Ga-core shuffle set Lomer dislocations nucleation could be easier. This may explain the higher fraction of Lomer dislocations in the (1–10) interface.

V. CONCLUSIONS

We have studied the mechanism for anisotropic strain relaxation in GaSb islands grown on GaP (001) substrate with a Ga-rich surface treatment at 480°C . In this highly mismatched system, the strain is relaxed predominately by Lomer dislocations and closely spaced 60° dislocation pairs which form at the interface. Therefore, using our growth conditions, a higher misfit strain relaxation was obtained along the island's elongation direction, which is in agreement with a higher density of misfit dislocations. It was shown that the anisotropy in the strain relaxation was related to the asymmetric configuration of interface misfit dislocations along the [1–10] and [110] directions. More specifically, the P-core glide set 60° dislocations (α type) and Ga-core shuffle set Lomer dislocations serve as the primary

misfit dislocations which contribute to the strain relaxation in the (1–10) interface and the Ga-core glide set 60° dislocations (β type) and P-core shuffle set Lomer dislocations for the (110) interface, respectively. The lower formation energy and higher glide velocity of the P-core glide set 60° dislocations (α type) result in a higher line density and more uniform periodical distribution of misfit dislocations in the (1–10) interface. The higher fraction of Lomer dislocations, which originated from the Ga-rich substrate surface and the discrepancy in the Lomer dislocations configuration stability, promotes a better strain relief in the (1–10) interface, with the corresponding elongation of islands in the [110] direction.

ACKNOWLEDGMENTS

This work is supported by the National Research Agency under Project MOS35, Contract No. ANR-08-NANO-022.

- ¹B. R. Bennett, R. Magno, J. B. Boos, W. Kruppa, and M. G. Ancona, *Solid-State Electron.* **49**, 1875 (2005).
- ²B. R. Bennett, *Appl. Phys. Lett.* **77**, 3736 (1998).
- ³S. El Kazzi, L. Desplanque, C. Coinon, Y. Wang, P. Ruterana, and X. Wallart, *Appl. Phys. Lett.* **97**, 192111 (2010).
- ⁴B. R. Bennett and J. A. del Alamo, *Appl. Phys. Lett.* **58**, 2979 (1991).
- ⁵M. Sugisaki, H. W. Ren, S. V. Nair, E. Tokunaga, K. Nishi, Y. Masumoto, and H. E. Ruda, *Phys. Rev. B* **75**, 125315 (2007).
- ⁶S. Lohr, S. Mendach, T. Vonau, Ch. Heyn, and W. Hansen, *Phys. Rev. B* **67**, 045309 (2003).
- ⁷A. Vila, A. Cornet, J. R. Morante, P. Ruterana, M. Loubradou, R. Bonnet, Y. Gonzalez, and L. Gonzalez, *Philos. Mag. A* **71**, 85 (1995).
- ⁸A. Vila, A. Cornet, J. R. Morante, P. Ruterana, M. Loubradou, R. Bonnet, *J. Appl. Phys.* **79**, 676 (1996).
- ⁹H. Suzuki, T. Sasaki, A. Sai, Y. Ohshita, I. Kamiya, M. Yamaguchi, M. Takahasi, and S. Fujikawa, *Appl. Phys. Lett.* **97**, 041906 (2011).
- ¹⁰O. Yastrubchak, T. Wosinski, J. Z. Domagala, E. Lusakowska, T. Figiel-ski, B. Peczek, and A. L. Toth, *J. Phys.: Condens. Matter* **16**, S1 (2004).
- ¹¹R. E. Mallard, P. R. Wilshaw, N. J. Mason, P. J. Walker, and G. R. Booker, *Inst. Phys. Conf. Ser.* **100**, 331 (1989).
- ¹²Y. Wang, P. Ruterana, L. Desplanque, S. El Kazzi, and X. Wallart, *J. Appl. Phys.* **109**, 023509 (2011).
- ¹³J. Narayan and S. Oktyabrsky, *J. Appl. Phys.* **92**, 7122 (2002).
- ¹⁴Q. H. Xie, A. Madhukar, P. Chen, and N. P. Kobayashi, *Phys. Rev. Lett.* **75**, 2542 (1995).
- ¹⁵Z. M. Wang, S. L. Feng, X. P. Yang, Z. D. Liu, Z. Y. Xu, H. Z. Zheng, F. L. Wang, P. D. Han, and X. F. Duan, *J. Cryst. Growth* **192**, 79 (1998).
- ¹⁶J. C. P. Chang, T. P. Chin, and J. M. Woodall, *Appl. Phys. Lett.* **69**, 981 (1996).
- ¹⁷H. Chen, L. C. Cai, C. L. Bao, J. H. Li, Q. Huang, and J. M. Zhou, *J. Cryst. Growth* **208**, 795 (2000).
- ¹⁸F. H. Stillinger and T. A. Weber, *Phys. Rev. B* **31**, 5262 (1985).
- ¹⁹W. Qian, M. Skowronski, R. Kaspi, M. De Graef, and V. P. Dravid, *J. Appl. Phys.* **81**, 7268 (1997).
- ²⁰S. H. Huang, G. Balakrishnan, and D. L. Huffaker, *J. Appl. Phys.* **105**, 103104 (2009).
- ²¹E. Steimetz, F. Schienle, J.-T. Zettler, and W. Richer, *J. Cryst. Growth* **170**, 208 (1997).
- ²²G. D. Li, C. Jiang, Q. S. Zhu, and H. Sakaki, *Appl. Phys. Lett.* **98**, 032103 (2011).
- ²³B. M. Kinder and E. M. Goldys, *Appl. Phys. Lett.* **73**, 1233 (1998).
- ²⁴J. C. Jiang, E. I. Meletis, Z. Yuan, and C. L. Chen, *Appl. Phys. Lett.* **90**, 051904 (2007).
- ²⁵A. Rocher, A. Ponchet, S. Blanc, and C. Fontaine, *Appl. Surf. Sci.* **188**, 55 (2002).
- ²⁶Th. Kehagias, Ph. Kominou, G. Nouet, P. Ruterana, and Th. Karakostas, *Phys. Rev. B* **64**, 195329 (2001).
- ²⁷M. J. Hytch, E. Snoek, and R. Kilaas, *Ultramicroscopy* **74**, 131 (1998).
- ²⁸S. Kret, P. Ruterana, A. Rosenauer, and D. Gerthsen, *Phys. Status Solidi B* **227**, 247 (2001).
- ²⁹N. Aichoune, V. Potin, P. Ruterana, A. Hairie, G. Nouet, and E. Paumier, *Comput. Mater. Sci.* **17**, 380 (2000).
- ³⁰P. Ruterana, B. Barbaray, A. Béré, P. Vermaut, A. Hairie, E. Paumier, G. Nouet, A. Salvador, A. Botchkarev, and H. Morkoç, *Phys. Rev. B* **59**, 15917 (1999).
- ³¹M. Ichimura, *Phys. Status Solidi A* **153**, 431 (1996).
- ³²Z. Q. Wang and D. Stroud, *Phys. Rev. B* **42**, 5353 (1990).
- ³³X. Zhou, J. Zhao, X. Chen, and W. Lu, *Phys. Rev. A* **72**, 053203 (2005).
- ³⁴H. P. Lei, J. Chen, and P. Ruterana, *J. Appl. Phys.* **108**, 103503 (2010).
- ³⁵J. Hornstra, *J. Phys. Chem. Solids* **5**, 129 (1958).
- ³⁶R. France, A. J. Patk, C.-S. Jiang, and S. P. Ahrenkiel, *J. Appl. Phys.* **107**, 103530 (2010).
- ³⁷I. Yonenaga and K. Sumino, *J. Cryst. Growth* **126**, 19 (1993).
- ³⁸P. J. van der Wel, J. te Nijenhuis, E. R. H. van Eck, and L. J. Giling, *Semicond. Sci. Technol.* **7**, A63 (1992).
- ³⁹L. Gelczuk, J. Serafinczuk, M. Dabrowska, and P. Dluzewski, *J. Cryst. Growth* **310**, 3014 (1993).
- ⁴⁰P. J. Parbrook, B. K. Tanner, B. Lunm, J. H. C. Hogg, A. M. Keir, and A. D. Johnson, *Appl. Phys. Lett.* **81**, 2773 (2002).
- ⁴¹W. M. Lomer, *Philos. Mag.* **42**, 1327 (1951).
- ⁴²S. Oktyabrsky and J. Narayan, *MRS Proc.* **399**, 443 (1996).